Available online at www.sciencedirect.com

ScienceDirect

Procedia CIRP 85 (2019) 102–107

www.elsevier.com/locate/procedia

2nd CIRP Conference on Composite Material Parts Manufacturing (CIRP-CCMPM 2019)

Computational Manufacturing for Multi-Material Lightweight Parts

André Hürkamp[a,c,*], Ralf Lorenz[b,c], Bernd-Arno Behrens[b,c], Klaus Dröder[a,c]

[a] *Technische Universität Braunschweig, Institute of Machine Tools and Production Technology, Langer Kamp 19b, 38106 Braunschweig, Germany*
[b] *Leibniz Universität Hannover, Institute of Forming Technology and Machines, An der Universität 2, 30823 Garbsen, Germany*
[c] *Open Hybrid LabFactory, Hermann-Münch-Straße 2, 38440 Wolfsburg, Germany*

Abstract

In this contribution, a computational approach for the manufacturing of multi-material lightweight parts is presented. For an efficient online optimization procedure, a proper orthogonal decomposition on offline obtained numerical results is carried out to construct a surrogate model. The functionality of the proposed framework is demonstrated on a use case study of a multi-material component consisting of a sheet metal basic structure and a plastic reinforcement structure. The manufacturing process chain consists of a deep drawing process followed by an injection molding process of short fiber reinforced plastics. The proposed methodology provides a fast and accurate computational model for structural properties with respect to the process settings.

Keywords: Composites; Simulation; Production planning; Finite element method (FEM)

1. Introduction

In the concept of multi-material design, different classes of materials are combined within one or more manufacturing steps. This enables a highly efficient use of material and an optimized structural design, [11]. Multi-material lightweight parts do not only contribute to an efficient material use for a load carrying structure, they also enable the integration of functions, [9]. Due to economic boundary conditions, such as material costs and cycle times, pure composite lightweight solutions are often not implementable in large scale production systems. Conventional pure steel solutions are economical but often limited in terms of weight reduction. Hence, multi-material solutions are promising alternatives, as they maintain the integration in large scale production, [17].

In this contribution, the virtual process chain for a generic multi-material part is investigated exemplary. It consists of a sheet metal cup and a reinforcing structure of a glass fiber reinforced thermoplastic. The geometry of the multi-material part is chosen for demonstration purposes following the geometries investigated in [8, 4]. The combination of both manufacturing steps – deep drawing and injections molding – shows great potential, since both processes are already established in large scale production industries such as the automotive industry.

Introducing lightweight parts as load carrying structures, numerical tools are required to describe the mechanical behavior of the composite during the design phase. An accurate material description taking into account effects such as material thinning or the fiber orientation due to the manufacturing process is mandatory to estimate strength and durability. The most frequently used method in computational engineering is the finite element method (FEM). The mechanical properties of the desired structure are mainly influenced by the manufacturing process. In order to take into account those influences for the structural design, the virtual process chain has to be considered for the finite element analysis (FEA) of the virtual prototype, [16]. With increasing complexity of the manufacturing process and the corresponding process chains, information has to be exchanged between different simulation steps. Thus, between each simulation step information in form of FEA results must be transferred to the subsequent analysis. In the industrial practice, this can take several days or weeks to analyze a complete process chain due to computation time, mapping of results, manual model updating and communication. Therefore, a holistic simulation environment in combination with physical meaningful reduced models is beneficial to overcome large computation times.

* Corresponding author. Tel.: +49 531 391-65044 ; fax: +49 531 391-5842.
E-mail address: a.huerkamp@tu-braunschweig.de (André Hürkamp).

2212-8271
10.1016/j.procir.2019.09.041

2. Reduced Order Modeling

Reduced order modeling (ROM) techniques approximate the solution of a physical system without simplifying the model and the underlying physics [7]. ROM is closely related to the field of surrogate modeling. Furthermore, an online feasible computation model allows the combination of ROM and data-science to get a direct feedback from e.g. process data.

In this work, we use a so-called a posteriori model reduction technique, where a parametric solution is computed during an offline phase. From this database an online feasible surrogate is built. In order to analyze the data of the offline generated results, proper orthogonal decomposition (POD) [6] is used here. POD is comparable to a principal component analysis [13]. An extension of POD is the proper generalized decomposition (PGD), [2]. PGD does not need any a priori knowledge of the solution in form of numerous offline computations. For example, it is used within a cyber physical system for predictive maintenance of a resin transfer molding process, [18]. However, within the PGD framework the reduced solution is computed simultaneously with the finite element problem. Such a procedure requires a special type of solver (e.g. the large time increment method [14]), that is not available in standard finite element software. Therefore, PGD is not well applicable in the field of computational manufacturing since different software solutions are coupled to solve the specific tasks of the manufacturing steps. Hence, using POD is advantageously in terms of implementation and independence of software packages and is applied in this contribution.

For POD, the numerical results obtained from detailed process simulations are used to build a reduced approximation. The field variables can either be element or nodal results. One solution vector for a fixed parameter α yields the result at the spatial coordinates $\mathbf{x}$ and is referred to as snapshot. The matrix of snapshots $\boldsymbol{\Upsilon}(\mathbf{x},\alpha) = [\upsilon_i(\mathbf{x},\alpha)\dots\upsilon_m(\mathbf{x},\alpha)]$ contains m solution vectors $\upsilon_i(\mathbf{x},\alpha)$ of detailed FEA. The size of $\boldsymbol{\Upsilon}(\alpha)$ is $n \times m$, where n denotes the number of element or nodal results contained.

Following the approach in [19, 12], the eigenvalue problem

$$(\mathbf{R} - \lambda_i \mathbf{I})\,\bar{\phi}_i = 0 \quad \text{with} \quad \mathbf{R} = \frac{1}{m}\boldsymbol{\Upsilon}^{\mathrm{T}}\boldsymbol{\Upsilon} \tag{1}$$

with λ_i denoting the eigenvalues and the corresponding eigenvectors $\bar{\phi}_i$ has to be solved. By normalizing $\phi_i = \boldsymbol{\Upsilon}\bar{\phi}_i/\|\boldsymbol{\Upsilon}\bar{\phi}_i\|$, the reduced representation

$$\mathbf{U}^{\alpha}(\mathbf{x},\alpha) \approx \sum_{i=1}^{k} \phi_i(\mathbf{x}) \cdot \lambda_i(\alpha), \tag{2}$$

is given. Thereby, the vectors $\phi_i(\mathbf{x})$ build a basis for the reduced solution. They are referred to as spatial modes and depend only on the spatial coordinates $\mathbf{x}$. The scalar functions $\lambda_i(\alpha)$ depend only on the parameter α. In general, there is no restriction on α. Parameters of interest could be e.g. geometric dimensions, the position of boundary conditions, the position and magnitude of loads, material properties and process parameters. For $k < m$, the series expansion (2) yields a reduced representation of the FEA result.

Table 1. Material Properties of DX56

Density ρ	Young's Modulus E	Poisson's ratio ν	Yield Stress $R_{p0.2}$
7.8 g/cm^3	211 GPa	0.29	172 MPa

3. Numerical Results

As an example, a multi-material structure is investigated numerically. First, the deep drawing process for a sheet metal cup is analyzed using LS-DYNA [15]. Subsequently, an injection molding simulation for the plastic part is carried out in the software Moldflow [3]. Based on the numerical results, a reduced order process model is obtained.

3.1. Deep drawing process

Deep drawing is one of the most important sheet metal forming processes and represents a key factor for the weight reduction, e.g. as an interface for combination to other manufacturing processes [5].

3.1.1. Parametric study on deep drawing

The deep drawing simulation was set up in the software LS-DYNA [15] using an explicit solver. The corresponding model and the dimensions of the blank are shown in Fig. 1. The final deep drawn cup is of dimension $180\,mm \times 100\,mm \times 40\,mm$.

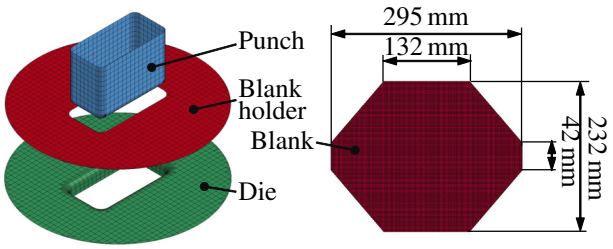

Fig. 1. Simulation model of the deep drawing process

The displayed tool consists of blank holder, die and rectangular punch modeled as shell elements. The sheet metal blank is clamped between blank holder and die with a defined force F_{bh} which has been varied within this study between 50 kN and 200 kN. During the test procedure, the punch is deep drawing the blank with a constant speed of $v = 20\,\mathrm{mm\,s^{-1}}$ through the cavity up to a drawing depth of $h = 40$ mm. All tools are modeled as rigid bodies. The frictional contact between blank and tool has been modeled with a constant friction coefficient of $\mu = 0.15$. For the blank material, a conventional deep drawing steel DX56 has been characterized by experimental tensile tests. The flow behavior is described by the Ghosh flow curve $k_f(\varphi) = 2115 \cdot (0.01366 + \varphi)^{0.04191} - 1620$ MPa, where φ denotes the effective plastic strain, [20].

For the material model, MAT_24 available in LS-Dyna has been applied. It describes an elasto-plastic material behavior with an arbitrary stress versus strain curve and strain rate dependency, [15]. The mechanical properties of the sheet metal are summarized in Table 1.

3.1.2. Results of the parametric study

For the reduced order process model the last stage of each deep drawing simulation was evaluated. Therefore, the nodal coordinates are plotted. Furthermore, for each element of the blank the parameters effective plastic strain, von Mises stress and the shell thickness have been exported. It can be observed that with increasing blank holder force the material flows dominantly out of the sheet thickness and less out of the sheet plane. For this reason, individual elements stretch more extensively. In the case of shell thickness, differences can be observed in different areas of the cup. In order to get an overview of the distribution of the sheet thickness, the global maximum and minimum values of each computed cup are summarized in Fig. 2.

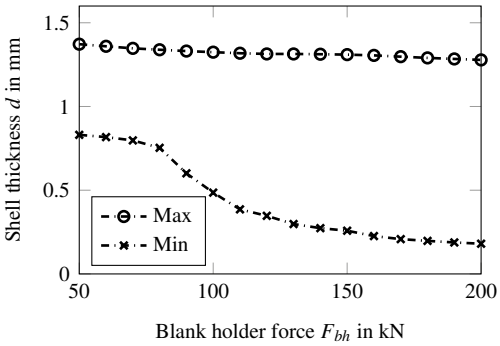

Fig. 2. Shell thickness d vs. blank holder force F_{bh}

Due to the reduction of radial and tangential stresses in the flange, the maximum and the minimum shell thickness are decreasing with increasing forces. The minimum shell thickness strongly decreases between $F_{bh} = 90\,\text{kN}$ and $F_{bh} = 110\,\text{kN}$. In this area, the cup wall begins to thin more strongly.

3.2. Injection Molding

For the analysis of the injection molding process, we use a Polyamid 6 with 30 mass-% glass fibers. The fluid flow is described by the Cross-WLF viscosity model, [21]. Therein the melt viscosity

$$\eta = \frac{\eta_0}{1 + \frac{\eta_0 \dot{\gamma}}{\tau^*}^{1-n}} \tag{3}$$

is described by the shear rate $\dot{\gamma}$, an critical stress level τ^* and a power law index n. The Newtonian limit

$$\eta_0 = D_1 \exp\left[-\frac{A_1(T - T^*)}{A_2 + (T - T^*)}\right] \tag{4}$$

with $A_2 = A_3 + D_3\, p$ and the glass transition temperature $T^* = D_2 + D_3\, p$ is described by the material specific coefficients A_1, A_3, D_1, D_2, D_3 and the pressure p. The material data used in this study are given in table 2. The geometrical model consists of two volume bodies representing the mold cavity (black) and the metallic insert part (gray). For both parts, tetrahedral elements are used, where the mold cavity is discretized with eight elements over the wall thickness to ensure a fine grid for the plastic flow analysis. The injection location (yellow) is placed in the center.

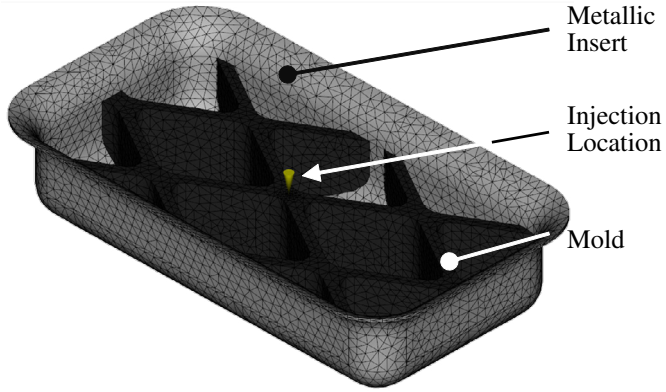

Fig. 3. Moldflow model

In order to prevent a drastic increase in the number of snapshots needed in the offline phase, the reduction of the wall thickness is not considered in the injection molding simulation. Consequently, the sheet metal insert has been modeled with a constant sheet thickness d =1.2 mm. With such modeling no direct coupling between the deep drawing and injection molding exists in the virtual process chain. However, the results of the individual processes can be combined arbitrarily for further investigations. In order to prevent a fast cooling of the plastic melt when in contact with the metallic insert, the initial temperature is set constant to $T_{insert} = 200\,°\text{C}$. The contact time between tool and insert is 2 s before the injection starts. The mold surface temperature is constant $T_{mold} = 100\,°\text{C}$ and the melt temperature of the plastic is $T_{melt} = 280\,°\text{C}$. For the parametric study, the injection time t_{inj} has been varied between 0.5 s and 20 s.

The mechanical behavior of the final structure is mainly determined by the fiber orientation **a** within the FRTP component. In the numerical analysis it is computed by Folgar-Tucker model [10] with a fiber interaction coefficient of $c_a = 0.0156$. In total 23 simulation results are obtained. For each simulation result, the tensor of fiber orientation **a**, exemplary depicted in Fig. 4, is exported and used for the following model order reduction.

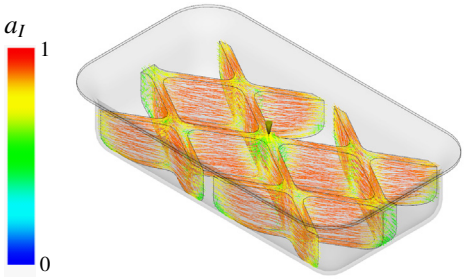

Fig. 4. First eigenvector a_I of the orientation tensor **a** for $t_{inj} = 2\,\text{s}$.

3.3. Reduced order process model

The FEA results from the parametric studies are used for the reduced process model. Form the deep drawing process 16 snapshots and from the injection molding process 23 snapshots are available to build the matrices Υ^u for the nodal displacement

Table 2. Cross-WLF coefficients from the Moldflow material database [3]

n	τ^*	D_1	D_2	D_3	A_1	A_3
0.42	78.3 kPa	4.78e+12 kPa s	323 K	0 K/kPa	37.2	51.6 K

of the sheet metal blank, Υ^d for the element thickness, and Υ^a for the fiber orientation due to the injection molding. Solving the corresponding eigenvalue problem (Eq. 1) yields following POD representation for the displacement

$$\mathbf{U}^u(\mathbf{x}, F_{bh}) \approx \sum_{i=1}^{k} \lambda_i^u(F_{bh}) \cdot \phi_i^u(\mathbf{x}) \tag{5}$$

and for the element thickness

$$\mathbf{U}^d(\mathbf{x}, F_{bh}) \approx \sum_{i=1}^{k} \lambda_i^d(F_{bh}) \cdot \phi_i^d(\mathbf{x}). \tag{6}$$

The resulting spatial modes are displayed in Fig. 5. In the contour plot the vector norm $\|\phi_i^u(\mathbf{x})\|$ is displayed. Hence, the contour plots correspond to the magnitude of displacement. The comparison of the first mode with the obtained final geometry yields a strong correlation to the actual displacement. Below the spatial mode, the scalar function $\lambda_1^u(F_{bh})$ is plotted. Here we observe a monotonically decreasing function, which yields a decrease of influence of the first spatial mode with increasing blank holder force F_{bh}. However, the first mode is still the main factor for the design of the reduced model. The absolute value of λ_1^d is in the range of 10^3, whereas the remaining functions show a maximum peak-to-peak amplitude between −400 and 400. Taking a look into the diagram for λ_4^d, a significant peak occurs at $F_{bh} = 160\,\text{kN}$. This observation implies that the 4th mode contains a feature specific to the result for $F_{bh} = 160\,\text{kN}$.

The scalar functions $\lambda_i^d(F_{bh})$ for the sheet thickness depicted in Fig. 6 are qualitatively similar to $\lambda_i^u(F_{bh})$, Here we also observe the significant peak in the 4th function. The spatial modes $\phi_i^u(\mathbf{x})$ are mapped onto the initial blank and represent the sheet metal thickness d. The thinning during the deep drawing process occurs mainly at the wall of the cup. In case of large blank holder forces, the thinning becomes critical and a localization of plastic strain is observed in the numerical results.

Analogous to the results from the deep drawing simulation, the reduced approximation of the fiber orientation **a** from the injection molding simulation can be specified to

$$\mathbf{U}^a(\mathbf{x}, t_{inj}) \approx \sum_{i=1}^{k} \lambda_i^a(t_{inj}) \cdot \phi_i(\mathbf{x}). \tag{7}$$

The first four scalar functions are displayed in Fig. 7. Similar to the reduction of the deep drawing, the absolute value of the first function is significantly larger than for the other three functions. This corresponds to the spatial mode for the fiber orientation. In Fig. 7 the first 4 spatial modes $\phi_i^a(\mathbf{x})$ are displayed. The contour plot represents the spatial modes for the largest eigenvalue a_I of the fiber orientation. Comparing the first mode with the fiber orientation obtained from the example in Fig. 4, a strong agreement is observed. This leads to the assumption that mainly the first mode of the reduced model represents the fiber orientation.

3.4. Error Analysis

In order to evaluate the number of modes $k \leq m$ needed for a sufficient approximation, we determine the error

$$\eta^\alpha = \|\mathbf{U}_{red}^\alpha - \mathbf{U}^\alpha\| / \|\mathbf{U}^\alpha\|. \tag{8}$$

The error for the displacement after the deep drawing process is plotted in Fig. 8 (a), the error for the sheet thickness is depicted in Fig. 8 (b). In the diagrams, an error range is given, showing the smallest and largest error observed. With increasing number of modes k in Eq. (5) and Eq. (6), the error is decreasing. Choosing a relative error of 10^{-3} as a suitable convergence criteria, a sufficient representation of the displacement is obtained with 8 modes. For the sheet thickness, at least 10 modes should be considered to ensure a small error.

Fig. 8 (c) shows the approximation error for the estimated fiber orientation from the injection molding simulation. Also with increasing number of modes, the relative error decreases. However, for some examples using more than 20 modes shows still an error around 0.01. The slow convergence for the fiber orientation can be explained by the form of the scalar functions (cf. Fig. 7). The non-smooth course of the functions implies that either the number of snapshots is not large enough to find an appropriate approximation or the influence of the injection time is too small to be captured by POD.

In the error analysis of the reduced process model, all predefined samples have been considered for calculating the reduced basis. Hence, all solutions approximated by POD are part of the data set. In order to evaluate the potential of interpolation, certain snapshots are not considered in the matrix of snapshots. Since the spatial modes are independent of α, only the functions $\lambda(\alpha)_i$ has to be evaluated for a certain value α. Here we interpolate piecewise linear between the supporting points. In accordance with Eq. (8), we compute the error for the interpolated solution compared to the solution of a full FEA.

In Fig. 9 (a) the error for the deep drawing model is shown. A convergence of the error is observed for each sample. An error less than 10^{-3} cannot be achieved by interpolation. However using only three to seven modes yields an error less than 1%, which is a sufficient approximation to be used in online computations. The error for the fiber orientation depicted in Fig. 9 (b) is almost constant around 10%. In contrast to the deep drawing model, no suitable approximation can be computed by interpolating the scalar functions $\lambda(\alpha)_i$. As a result of this study, the database for the injection molding investigated seems not suitable for the presented model reduction approach. In further studies, the influence of the sample space and the number of snapshots has to be investigated in detail to increase the quality of the model reduction.

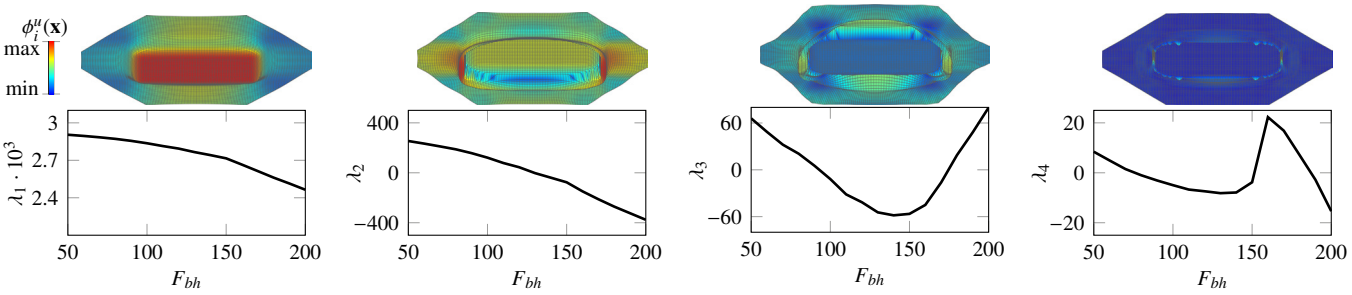

Fig. 5. POD modes for the displacement after the deep drawing process: spatial modes (top) and corresponding scalar functions (bottom)

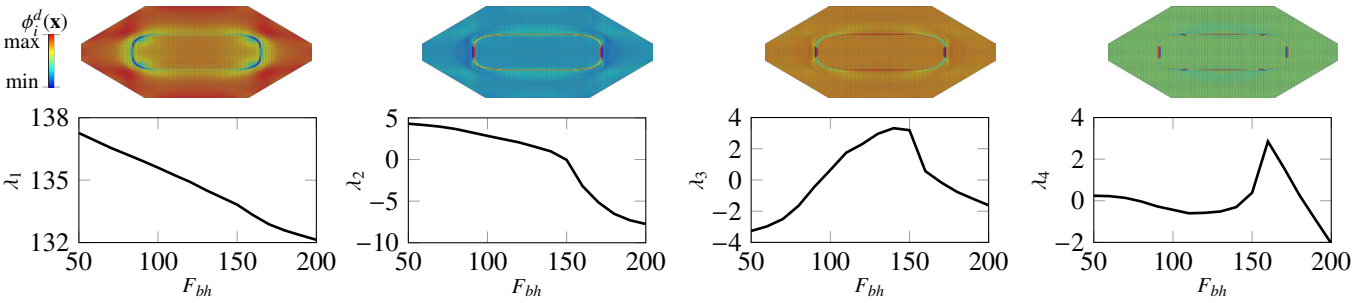

Fig. 6. POD modes for the sheet thickness at the end of the deep drawing process: spatial modes (top) and corresponding scalar functions (bottom)

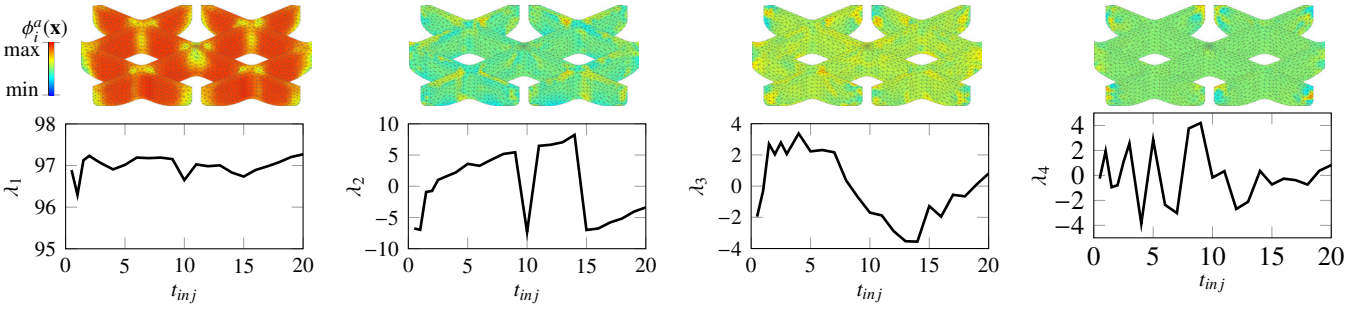

Fig. 7. POD modes for the fiber orientation: spatial modes representing the first eigenvalue of the orientation tensor (top) and corresponding scalar functions (bottom)

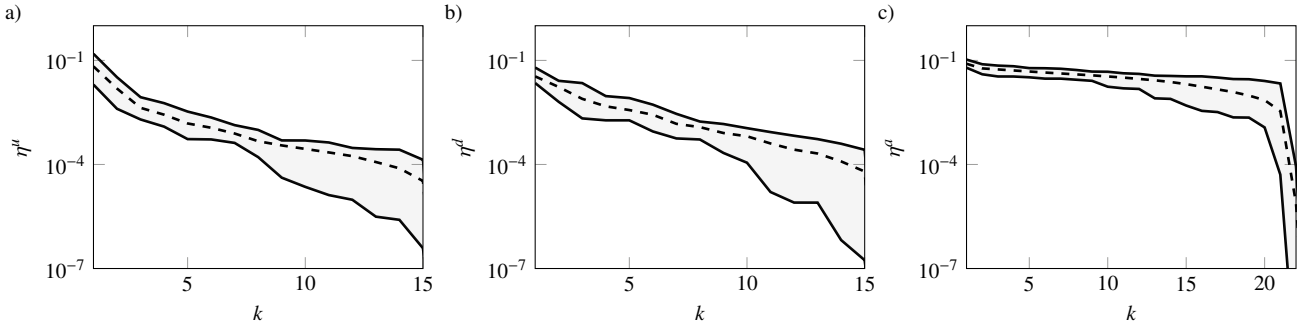

Fig. 8. Error of the model reduction compared to the full model: a) error of displacement u, b) error of sheet thickness d, c) error of fiber orientation $\mathbf{a}$

4. Concluding Remarks

In this paper, a reduced order process model based on POD has been presented. As an example, the manufacturing process of a multi-material lightweight part has been investigated numerically. The process chain consists of the two steps deep drawing and injection molding. Using the data from parametric FEA results obtained in an offline phase, a reduced solution in form of a series expansion can be computed. Such a formulation allows to compute the solution of a virtual manufacturing process for different parameters in real time. In the present use case, the reduced order process model of the deep drawing leads to smaller approximation errors than the model of the injection molding. With the presented reduced order process model at hand final geometry, sheet thickness and fiber orientation can be given as an parametric input for the structural analysis of the multi-material lightweight part.

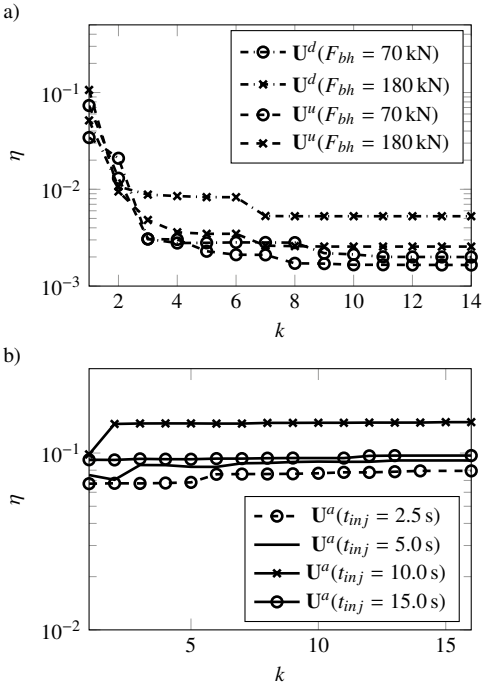

Fig. 9. Relative error for interpolated data: a) error of the interpolated deep drawing model and b) error of the interpolated injection molding model

In this investigation no direct coupling was realized between the two process steps. For an accurate description, this coupling has to be considered for the design of the reduced order model. Such a coupling will increase the parameter space so that sampling methods have to be applied in order to avoid a full factorial computational design of experiments during the offline phase. For a holistic computational production planning, information obtained on different levels (e.g. manufacturing and prototyping) has to be transferred into surrogate models for an integrated computational product and production planning (icPPP). In addition, online feasible surrogates in combination with real time process data can be used during the production phase for an inline quality control.

Acknowledgements

This research and results published are based on the research program Mobilise funded by the Ministry of Science and Culture of Lower Saxony and the Volkswagen Foundation.

References

[1] Advani, S.G., Tucker, C.L., 1987. The Use of Tensors to Describe and Predict Fiber Orientation in Short Fiber Composites: Journal of Rheology. Journal of Rheology 31, 751–784. doi:10.1122/1.549945.

[2] Ammar, A., Mokdad, B., Chinesta, F., Keunings, R., 2006. A new family of solvers for some classes of multidimensional partial differential equations encountered in kinetic theory modeling of complex fluids. Journal of Non-Newtonian Fluid Mechanics 139, 153–176. doi:10.1016/j.jnnfm.2006.07.007.

[3] Autodesk, 2017. Moldflow Insight.

[4] Bader, B., Berlin, W., Demes, M., 2019. Improvement of Lightweight Design Quality through Interdisciplinary Cooperation. Lightweight Design worldwide 12, 38–43. doi:10.1007/s41777-019-0024-5.

[5] Behrens, B.A., Hübner, S., Chugreev, A., Neumann, A., Grbic, N., Schulze, H., Lorenz, R., Micke, M., Bohne, F., 2019. Develeopment and numerical validation of combined forming processes for production of hybrid parts, in: Dröder, K., Vietor, T. (Eds.), Technologies for economical and functional lightweight design, Springer Berlin Heidelberg. pp. 29–39.

[6] Berkooz, G., Holmes, P., Lumley, J.L., 1993. The proper orthogonal decomposition in the analysis of turbulent flows. Annual review of fluid mechanics 25, 539–575.

[7] Chinesta, F., Cueto, E., Abisset-Chavanne, E., Duval, J.L., Khaldi, F.E., 2018. Virtual, Digital and Hybrid Twins: A New Paradigm in Data-Based Engineering and Engineered Data. Archives of Computational Methods in Engineering doi:10.1007/s11831-018-9301-4.

[8] Droste, A., Naughton, P., Bowser, B., Röttger, J., Burr, S., Imam, O., Zeitler, M., Heuft, T., Cawley, A., 2003. Bonded metal-plastic composite structures, in: SPE Automotive Composite Conference, Troy, USA.

[9] Fleischer, J., Nieschlag, J., 2018. Introduction to CFRP-metal hybrids for lightweight structures. Production Engineering 12, 109–111. doi:10.1007/s11740-018-0825-0.

[10] Folgar, F., Charles L. Tucker III, 1984. Orientation Behavior of Fibers in Concentrated Suspensions. Journal of Reinforced Plastics and Composites 3, 98–119. doi:10.1177/073168448400300201.

[11] Hufenbach, W.A., Werner, J., Kiele, J., 2013. Elektromobilität in Ultraleichtbauweise. ATZextra 18, 42–46. doi:10.1365/s35778-013-0019-5.

[12] Hürkamp, A., Kaliske, M., 2015. A model reduction approach for hyperelastic materials based on Proper Orthogonal Decomposition. PAMM 15, 203–204. doi:10.1002/pamm.201510092.

[13] Kambhatla, N., Leen, T.K., 1997. Dimension Reduction by Local Principal Component Analysis. Neural Computation 9, 1493–1516. doi:10.1162/neco.1997.9.7.1493.

[14] Ladevèze, P., 2012. Nonlinear computational structural mechanics: new approaches and non-incremental methods of calculation. Springer Science & Business Media.

[15] Livermore Software Technology Corporation, 2018. LS-DYNA.

[16] Masseria, F., Berger, A., Kaiser, B., 2015. Virtual Composite Manufacturing Simulation Chain, in: 20th Symposium on Composites, Trans Tech Publications. pp. 671–676.

[17] Modler, N., Hufenbach, W., Cherif, C., Ulbricht, V., Gude, M., Maron, B., Weck, D., Filippatos, A., Wiemer, H., Langkamp, A., 2016. Novel Hybrid Yarn Textile Thermoplastic Composites for Function-Integrating Multi-Material Lightweight Design. Advanced Engineering Materials 18, 361–368. doi:10.1002/adem.201600028.

[18] Quaranta, G., Abisset-Chavanne, E., Chinesta, F., Duval, J.L., 2018. A cyber physical system approach for composite part: From smart manufacturing to predictive maintenance. AIP Conference Proceedings 1960, 020025. doi:10.1063/1.5034826.

[19] Radermacher, A., Reese, S., Hadoush, A.M.H., 2013. Selective proper orthogonal decomposition model reduction for forming simulations. PAMM 13, 115–116. doi:10.1002/pamm.201310053.

[20] Werber, A., Liewald, M., Nester, W., Grünbaum, M., Wiegand, K., Simon, J., Timm, J., Hotz, W., 2013. Assessment of forming limit stress curves as failure criterion for non-proportional forming processes. Production Engineering 7, 213–221. doi:10.1007/s11740-013-0446-6.

[21] Williams, M.L., Landel, R.F., Ferry, J.D., 1955. The Temperature Dependence of Relaxation Mechanisms in Amorphous Polymers and Other Glass-forming Liquids. Journal of the American Chemical Society 77, 3701–3707. doi:10.1021/ja01619a008.